Global Contraction/Expansion and Polar Lithospheric Thinning on Titan from Patterns of Tectonism

A Thesis

Presented in Partial Fulfilment of the Requirements for the

Degree of Master's

with a

Major in Physics

in the

College of Graduate Studies

University of Idaho

by

Casey Ann Cook

May 2014

Major Professor: Jason Barnes, Ph.D.

Authorization To Submit Thesis

This thesis of Casey Cook, submitted for the degree of Master of Science with a major in Physics and titled "Global Contraction/Expansion and Polar Lithospheric Thinning on Titan from Patterns of Tectonism," has been reviewed in final form. Permission, as indicated by the signatures and dates given below, is now granted to submit final copies to the College of Graduate Studies for approval.

Major Professor _____Date_____
Jason Barnes, Ph.D.

Committee Members _____Date_____
Matthew Hedman, Ph.D.

_____Date_____
Simon Kattenhorn, Ph.D.

Department Administrator _____Date_____
Dave McIlroy, Ph.D.

Discipline's College Dean _____Date_____
Paul Joyce, Ph.D.

Final Approval and Acceptance by the College of Graduate Studies

_____Date_____
Jie Chen, Ph.D.

Abstract

We investigate the underlying physical processes that govern the formation and evolution of Titan's tectonic features. Our mapping of mountain chains and hills reveals a global pattern: east-west orientations at the equator and north-south at the poles. This result makes Titan one of the few solar system bodies where global processes, rather than regional processes, dominate tectonism. After comparison with global stress models, we suggest that either global contraction coupled with spin-up or global expansion coupled with despinning could explain our observations if coupled with a lithosphere thinner in Titan's polar regions.

Acknowledgements

I would like to thank Dr. Jason Barnes for his continued support and guidance during my time as a graduate student. I would also like to thank the collaborators of this work. I thank NASA Outer Planets Research Program grant NNX10AQ10G for the funding needed to produce this paper.

Table of Contents

List of Figures

Chapter 1 Background Introduction

This thesis is a result of work with collaborators that resulted in the Journal of Geophysical Research-Planets publication *Global Contraction/Expansion and Polar Lithospheric Thinning on Titan from Patterns of Tectonism.* The co-authors, Jason W. Barnes, Simon A. Kattenhorn, Terry Hurford, Jani Radebaugh, Bryan Stiles, and Mikael Beuthe, of the said publication assisted in the completion of this research. Specifically, J.W. Barnes, S.A. Kattenhorn, and J. Radebaugh provided Physics and Geological guidance when analyzing the tectonic mechanisms driving the formation of Titan's mountain chains and hills. Terry Hurford assisted in the formation of the following stress models: Global Expansion/Contraction, Change in Rotation Rate, and Global Expansion/Contraction with cahnge in Rotation Rate. Mikael Beuthe provided the models for the stress field as a result of Global Expansion/Contraction with Change in Rotation Rate and a variation in lithospheric thickness. Finally, Bryan Stiles provided the SARTopo data used to confirm changes in surface heights.

Chapter 2 Introduction

Several moons in our solar system display patterns of tectonism that are driven or modified by global forces ([14]). Europa's tidally induced fracture patterns ([18], [19], [21], [33]), Enceladus's tiger stripes ([41], [47], [48], [37], [34]), Ganymede's global-expansion-induced normal fault bands ([10], [20], [32], [49]), and Io's plain ridges ([8]) are examples of such tectonic patterns.

Given its eccentric orbit, proximity to Saturn, and numerous mountain chains, global stresses may affect Titan as well. Images taken with the RADAR Mapper (hereafter, *Cassini* RADAR) aboard the *Cassini* spacecraft have revealed features of high topography referred to as mountains in [39]. While the surfaces of Ganymede and Callisto—both of which have comparable size and mass to Titan—are dominated by impact craters, the large scale coherence of Titan's high topographic features suggests probable formation by global forces ([28] and [39]).

Synthetic Aperture RADAR (SAR) imagery obtained by *Cassini* RADAR, along with derived topographic information, show evidence for possible contractional or extensional tectonism within Titan's equatorial and polar regions as suggested by [28], [46], [13], and [40]. At the landscape scale, Titan's fluvial networks include rectangular or trellis morphologies, suggesting formation affected by tectonic structures ([13]). [28] propose that isotropic stress from radial contraction combined with stress from rotational spin-up, would favor the formation of mountain chains in the east-west direction in the equatorial region—like those observed on Titan with both the *Cassini* RADAR ([28], [39]) and Visual and Infrared Mapping Spectrometer (VIMS) data ([3]). However, Titan's mountains are globally pervasive, implying that a contraction/spin-up model alone is insufficient to explain the global pattern of tectonism.

In this study, we explore the possibility that Titan's tectonism is globally controlled. To do so, we first use *Cassini* RADAR images to map Titan's mountain

chains as described in Section 2. Section 3 describes how we use the mapping data to look for global patterns in the mountain chain orientations, which we then analyze and compare with possible formation mechanisms. Lastly, in Section 4, we interpret the geophysical implications of the mountain chains and their orientations in order to create a higher-order picture of the forces affecting Titan's tectonic features and their evolution.

Chapter 3 Mountain Observations

We construct the maps that we use in this research from a low resolution cylindrical base map raster ([5]) layered with higher resolution *Cassini* VIMS images ([4]) and *Cassini* RADAR swaths from the T3 through T69 flybys ([31]) (Figure 3.1). We aim to create a global map of the orientations of mountain chains in order to identify the mechanisms driving tectonism on Titan. Therefore, we include surface features that are identified as topographically high and possess a clear bright-dark pairing within *Cassini* RADAR in our mapping.

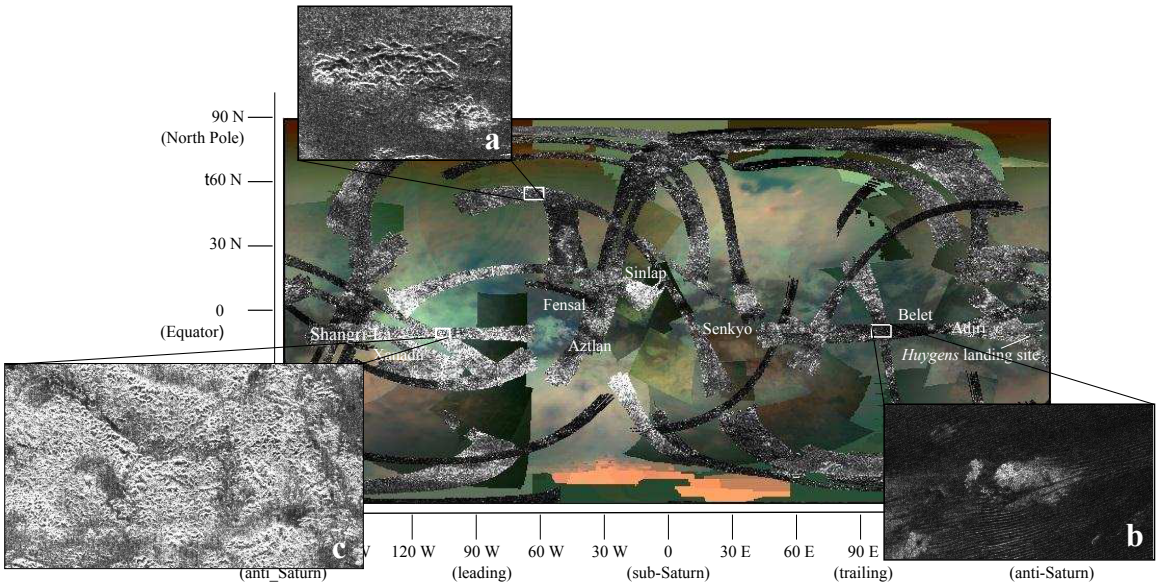

Figure 3.1: Global cylindrical map of Titan, annotated (names are all IAU accepted), highlighting the two categories of topographic uplifts discussed in this study, as well as a third category, the separately mapped Xanadu region. a. This mountain chain, known as Misty Montes, is located on *Cassini* RADAR swath T23 at approximately 62°N, 57°W. b. This example of Titan hills, named Arwen Colles, is located within the T8 *Cassini* RADAR swath at approximately 8°S, 100°E. c. Centered at approximately 10°S, 103°W, this image is part of the T13 *Cassini* RADAR swath and exemplifies the type of terrain that makes up the Xanadu region.

3.0.1 Cassini RADAR

Using microwaves instead of visible wavelengths, *Cassini* RADAR actively scans the surface of Titan measuring reflectivity using both passive (radiometry) and active (synthetic aperture, scatterometry, and altimetry) modes (Figure 3.2). As the spacecraft scans Titan's surface, it receives backscatter from each transmitted pulse. Recording the time it takes for the outgoing pulse to be returned to the spacecraft and the wavelength of the returned pulse, *Cassini* RADAR in the SAR mode produces images of highest intensity for a backscattering surface and lower for a forward-scattering or absorbing one ([3]).

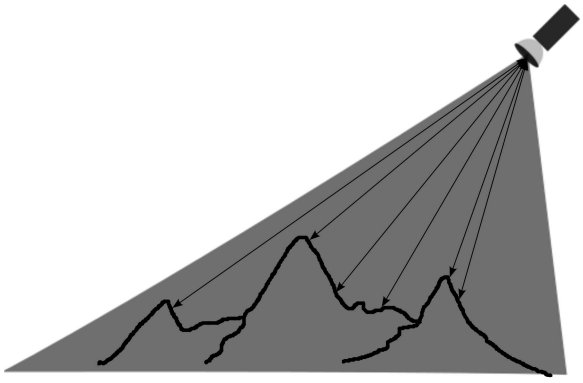

Figure 3.2: Conceptual illustration of how *Cassini* RADAR maps Titan's surface. For mountains, like those shown in the figure, as the outgoing radar beam hits the forward slope of a mountain, the time for the beam to return to the spacecraft is recorded and illustrated as a bright feature. The backward slope of the mountain, however, does not record a backscatter and is therefore recorded as a dark feature. This change in intensities is what composes a bright-dark pair and is characteristic of the topographic shading or sharp topographic boundary.

As discussed in [3], the intensity of the backscatter is a combination of the surface reflection (surface roughness and dielectric constant, and orientation relative to the beam) and a subsurface or volume scattering component (dependent on the number density and size of scatterers, the absorptivity of the matrix material, and the dielectric contrast between the matrix and scatterers).

In SAR mode, *Cassini* RADAR looks to the side instead of straight down. That geometry allows it to determine the distance from the spacecraft for each part of the return pulse based on the light travel time delay. This process works well for flat surfaces.

For mountains, like those shown in figure 3.2, as the outgoing radar beam hits the forward slope of a mountain, the beam is reflected back to the spacecraft and is thus recorded as a bright feature. This high intensity, bright characteristic is a product of radar backscatter for beams reaching the spacecraft at the same time. The back slope of the mountain, however, does not return backscatter (or does so over an extended time) and is therefore recorded at a lower intensity, producing a dark feature. This change in intensities is recorded as a bright-dark pair and is characteristic of the topographic shading or a sharp topographic boundary ([15] and [39]). All mountain chains and hills are therefore identified and mapped using *Cassini* RADAR data in this study, with the bright-dark pairing characteristic considered diagnostic.

3.0.2 Mountain Chains

Two distinct categories of tectonically formed topographic highs are apparent in *Cassini* RADAR data (Figure 3.1). The first are those that we define as mountain chains, as exemplified in Figure 3.1a. Features defined in this category possess a clear bright-dark pairing, a result from SAR illumination of the *Cassini* RADAR-facing slope and shading on the opposite slope. These mountain chains are generally between 70 and 100 kilometers in length and possess a long, linear nature that is unusual in the solar system other than on Earth.

To avoid error from exogenously formed mountain-like features, like those that define a crater ring, we only map mountain chains that display a linear nature and are clear of known craters (Sinlap ([24]), Selk ([44]), Paxsi ([12]), Afekan, and others

as discussed in [29]).

3.0.3 Hills

The second category of topographic highs observed in this study is hills. A hill's descriptor term collis (or plural: colles) is defined by the International Astronomical Union (IAU) as a small hill or knob (Figure 3.1b). Approximately 18% of Titan's surface is covered by dune fields ([26], [17]). The hills that are identified in this study are located within the dune fields, primarily in Titan's equatorial latitudes. These features are thought to be of higher surface elevation than the topography that surrounds them based on the redistribution of the surrounding dunes. At this time it is not evident why the hills primarily populate the dune fields. It is possible, however, that the high contrast between the dunes and the hills creates a visual bias and therefore hills are also located at higher latitudes, but not visible. High erosion rates and/or dune material may have helped shape the hills.

3.0.4 Xanadu

The Xanadu region (Figure 3.1c) contains Titan's most rugged and mountainous terrain ([40]). We map this region separately to avoid introducing error into global mountain chain orientation measurements due to Xanadu's unique features and possible independent formation as suggested by, [23] and [11].

Chapter 4 Mapping and Orientations

We map all categories of Titan's topographic highs as polygons in ArcMap. We choose this method because these features encompass a certain coverage area and identification of the bright-dark pairing that characterizes the mountain chains, hills, and Xanadu mountains is dependent on the look direction of *Cassini* RADAR. The radar look direction is an important parameter when analyzing features with a preferred orientation because features may be enhanced or distorted through radar illumination. The method of mapping Titan's mountains as polygons is to eliminate the look direction bias when establishing orientations. We chose to quantify orientations by writing a separate program in C++ and input the data from the mapped polygon features from ArcMap.

4.0.5 Mapping

An exemplary mountain chain, named Misty Montes (Figure 4.3), is an illustration of the presumed tectonic features in the mountain chain category. These features are identified in *Cassini* RADAR by a bright-dark pairing; bright recording more backscatter than the dark. The bright green polygon outlines the lateral boundaries of the mountain chain, providing constraints on the dominant orientation of the mountains.

Titan hills are generally 15 to 50 kilometers in length. The hills shown in Figure 4.4 are known as Arwen Colles. Outlined in pink, all hills are marked with a polygon feature class in ArcMap. While these features form tear-drop shapes within the dunes, only features displaying nonlinear, marbleized bright-dark pairing are considered to make up a Titan hill.

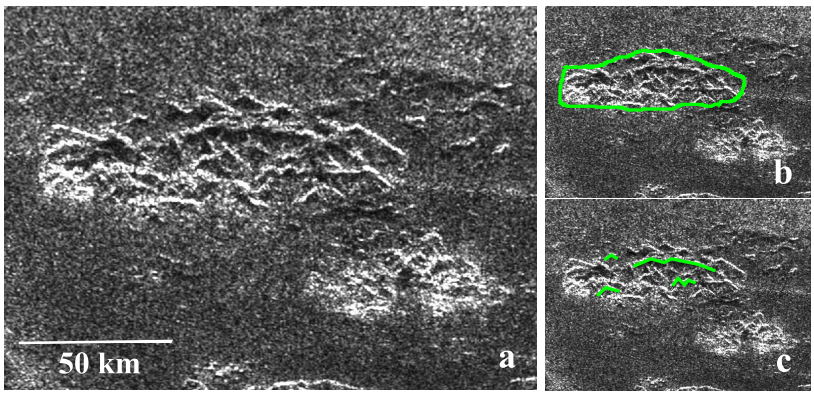

Figure 4.3: a. This exemplary mountain chain, known as Misty Montes, located in *Cassini* RADAR swath T23 and at approximately 57°N, 62°W, demonstrates the characteristic nature of tectonically formed mountain chains mapped in this research and identified in *Cassini* RADAR by a bright-dark pairing—bright indicating a higher level of backscatter than the dark. b. Outlined in green, all mapped mountain chains are marked with a polygon feature class in ArcMap. c. Green lines highlight the bright-dark pairing which characterizes mountain chains in *Cassini* RADAR.

In order to verify and provide supporting evidence for the validity of our mapped mountain chains and hills, we compare the data to the SARTopo imaging provided by Stiles (for more information on SARTopo, see [50]), where possible. A shift from bluer to redder colors, as defined by [50], is indicative of an increase in surface height (Figure 4.5).

Figure 4.5 verifies both types of Titan mountain categories. SARTopo imaging shows a color change from a cool blue to a warm yellow and turquoise when passing over the bright-dark pairing defined as the Titan mountain—indicating the feature is at a higher surface height than the terrain that surrounds it.

Similarly, SARTopo imaging shows a variation in color from a cool turquoise to a warm yellow when passing over the feature classified as the Titan hill. Like the mountain chain, the variation in color indicates an increase in surface height. Because surface height on Titan varies among regions, each mapped topographic feature is compared to the surrounding terrain as opposed to a baseline surface elevation for

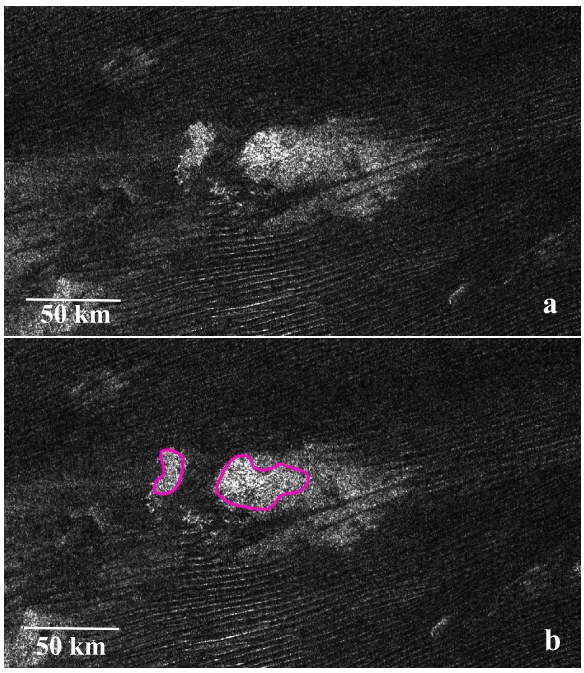

Figure 4.4: Within the sand dunes in Titan's equatorial latitudes are features described in this paper as hills. These hills are identified by the re-distribution of the dune field and a marbling effect of bright-dark pairing and are assumed to be of higher surface elevation than the topography that surrounds them. a. This example of Titan hills, known as Arwen Colles, sits within the T8 swath at approximately 8°S, 100°E. b. Outlined in pink, all hills are marked with a polygon feature class in ArcMap. To avoid error in mapping, only features displaying nonlinear bright-dark pairing were considered to make up the Titan hill.

all of Titan.

We focus our mapping of the Xanadu region on unambiguous topographic features displaying clear bright-dark pairings (Figure 4.6). These features share similar characteristics with those defined in the mountain chain category discussed above and is based on the SARTopo images. Figure 4.6b demonstrates an increase in surface height over features possessing clear bright-dark pairings, as indicated by the change from a cool blue to a warm yellow. Xanadu mountains are mapped as a polygon feature class in ArcMap with a dark green outline.

Figure 4.7 shows our global cylindrical map of the mapped mountain chains and hills without the VIMS images or *Cassini* RADAR swaths as background. The pink,

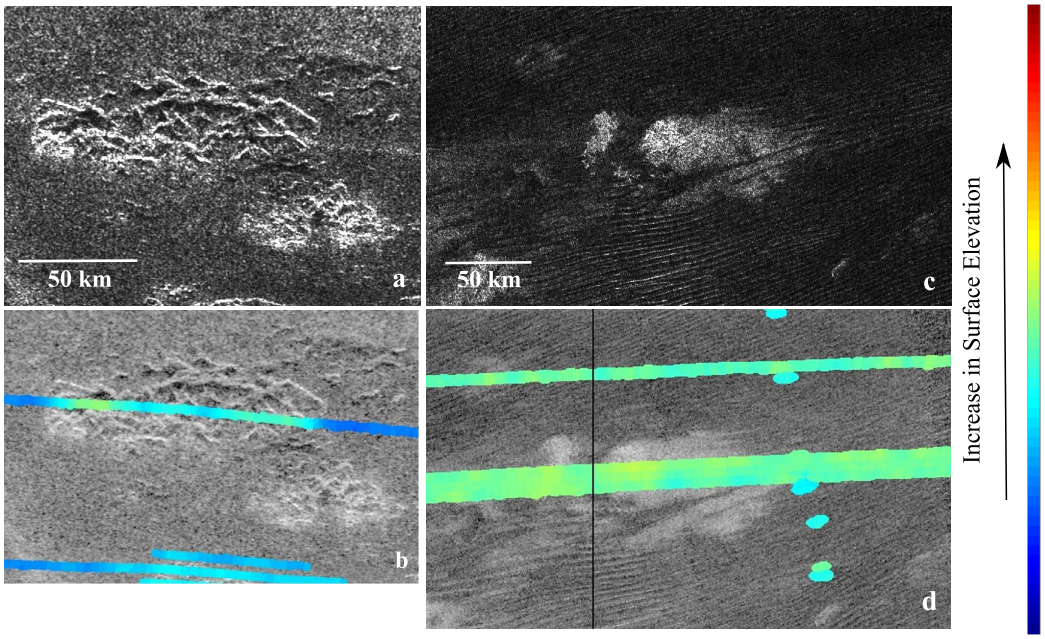

Figure 4.5: Verification of mountain chains and hills using SARTopo imaging. a. Misty Montes (Figure 4.3) b. The SARTopo image shows a color change over Misty Montes, a cool blue to a warm yellow and turquoise, indicative of an increase in surface height. c. Arwin Colles (Figure 4.4) d. The SARTopo image shows a variation in color from a cool turquoise over the dunes to a warm yellow over the feature classified as hills. This variation is indicative of an increase in surface height, verifying our identification of the area as a hill.

bright green, and dark green polygon features denote the mountains interpreted to be tectonic in origin. The purple polygon features are those mountain chains and hills that are confirmed by SARTopo to be of a higher surface elevation than the surrounding terrain.

4.0.6 Mountainorient

Our orientation program, deemed *Mountainorient*, calculates the orientation of the line between each vertex within an individual polygon. There is a median of 17 vertices among all the mapped polygons ranging from 5 to 236 vertices within a given polygon. The mathematical slope is determined using the x-y coordinates for each vertex within a given polygon, after a geometric correction for latitude. From

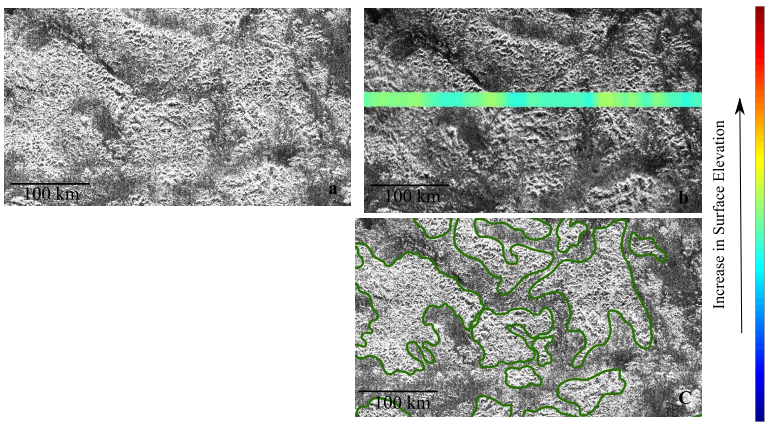

Figure 4.6: The region defined as Xanadu is composed of Titan's most rugged and mountainous terrain. Xanadu's mountain chains were mapped in a separate category due to their unique characteristics and possible independent formation. a. Part of *Cassini* RADAR swath T13 centered approximately at 10°S, 103°W, this image is an example of the terrain which comprises most of the Xanadu region. b. To avoid error in mapping, SARTopo data is used to determine areas of highest topography and therefore the best areas for mapping mountain ranges. As shown in this image, areas which display bright-dark pairing like that described in the mountain chain category, correspond to an increase in surface height. c. Mountain chains are mapped with a polygon feature class in ArcMap.

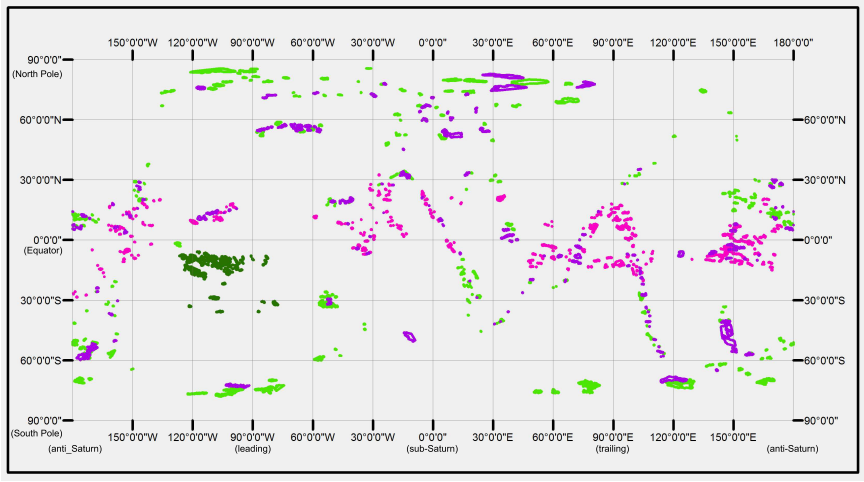

Figure 4.7: Global cylindrical map of Titan's mountains without the VIMS images and *Cassini* RADAR swaths as background. The pink, bright green, and dark green polygon features denote mountains identified to be tectonic in origin. Pink are defined as Titan hills, bright green are mountain chains, and dark green are those mountain chains mapped within the Xanadu region. The purple polygon features are those mountain chains and hills that have been identified using SARTopo data to be of a higher surface height than the surrounding terrain.

the mathematical slope, the angle is determined for each adjacent set of vertices. The orientation of the polygon is then determined by the mode angle of the vertices weighted by length. This orientation angle is then binned to form each rose diagram. The orientation angle for each polygon is measured from 0°N. This process is repeated separately for the mountain chain, hill, and Xanadu data.

Mountainorient then provides a rendering of the global spatial distribution of mountain chain observations by binning polygons within 30 degree square regions in longitude and latitude and creating a rose diagram. The two images in figure 4.8 are global maps of rose diagrams for the mountain chain category, including an inset of the separately mapped Xanadu region (Figure 4.8a), and hill category (Figure 4.8b). The area of each rose diagram is proportional to the area of polygons within each 30 degree square bin.

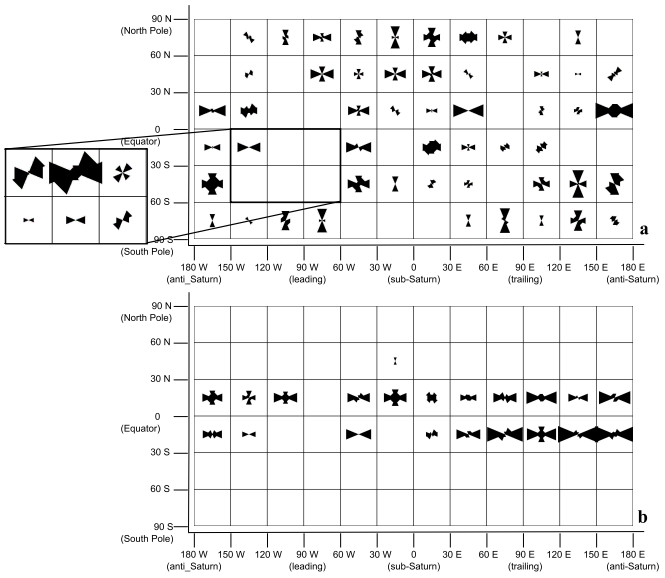

Figure 4.8: Global maps of rose diagrams for Titan's mountains. Orientations for the mountain chain category, including an inset of those mountains within the Xanadu region are shown in (a), while the hill category orientations are shown in (b). Each rose diagram is a result of binning mapped polygons into 30 degree square regions. From the global maps of rose diagrams, we note a trend of east-west orientation in Titan's equatorial regions changing to north-south orientation of the mountain chains at the poles.

Chapter 5 Analysis and Model

Quantitative results from *Mountainorient* show that both the mountain chains and hills have a higher tendency to be oriented east-west within 30 degrees of the equator, but mountain chains have a higher tendency to be oriented north-south between 60 degrees latitude and the poles. Nonetheless, exceptions to these dominant trends exist in both cases. For example, the 30 degree square bin lying in the north polar region between 60°W and 90°W shows mountain chain orientations trending east-west. Although we generalize both polar regions with north-south orientations, regions such as this may be explained by the presence of Titan's lakes and seas in this region— altering the landscape and therefore causing a mapping bias.

Mountain chains in the northern and southern mid-latitudes differ in orientations, however (Figure 4.8). While no distinct orientations can be assigned, there is a general trend of east-west orientations within the northern mid-latitudes and variably north-south, east-west, and SW-NE orientations within the southern mid-latitudes. Likewise, mountain chains within the Xanadu region display a quantified orientation varying between east-west and SW-NE. This non-distinct orientation may be explained as a result of Xanadu's origin as occupying the site of an ancient impact ([11]) and/or shaped by compressional and extensional tectonism with ongoing erosion from methane rainfall ([40]). Due to the observational differences between Xanadu and the mountains within the mountain category, the rose diagrams describing the Xanadu mountains are therefore left as an inset to figure 4.8a.

It should be noted that the observed mountain chains' orientations show a change from linear within the equatorial and mid-latitude regions to more equant at the poles (Figure 5.9). This morphological change may be as important as the orientation difference.

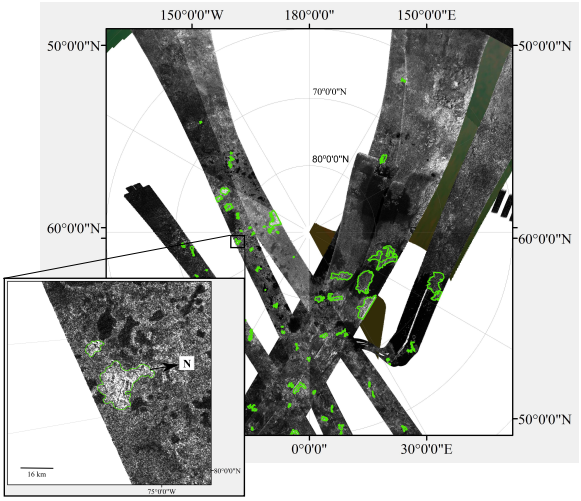

Figure 5.9: North polar projection of Titan in the region north of 60° latitude with mountain chains shown as green polygons. Located at 82°W, 79°N, the inset figure highlights examples of the less linear, more equant mountain chains that are prevalent in both the north and south polar regions.

Mountain chains can be formed through either compressional or extensional forces, as exemplified on Earth. For example, the Yakima Fold Belt within south-central Washington state, USA, is a system of wrinkle ridges that form linear mountain chains. These ridges are anticlines formed through the compression of flood basalt lavas that comprise the upper crust in the region. 'Thin-skinned' tectonic features such as these can also describe the fold-thrust belts of the Himalaya and the Appalachians. Contractional structures can also be formed by so-called 'thick-skinned' tectonics, in which the faults extend much deeper into the crust. The American Cordillera, which encompass the Rocky Mountains and stretch from southern South America up to Alaska, is an example of such a tectonic feature.

In contrast, linear mountain chains can also form through extension, like those within the Great Basin throughout Western North America. This basin and range region consists of a series of grabens and horsts formed by the stretching of the Earth's lithosphere with uplifted horst blocks creating the linear mountain ranges.

The morphological change in mountains on Titan could be a response to regional changes of compression and tension. Current imaging capabilities and high erosion

rates do not, however, afford us the ability to investigate Titan's surface with the detail required for fault distinctions. However, by looking at the theoretical stress orientations and magnitudes, we can make reasonable assumptions about the likelihood of mountains being related to faults in the ice shell caused by those stresses.

5.0.7 Global Stress Models

The existence of mountain chains in distinct orientations that are latitudinally dependent motivates us to test a range of plausible global stress conditions that can generate east-west trending mountains at the equator of a planet and north-south mountains at its poles. Figure 5.10 illustrates the relationship between the likely principal stresses and mountain orientations.

Gravitational tides, differentiation, orbital migration, and non-synchronous rotation can be ruled out as possible mechanisms forming the mountain chains and hills, since these do not produce stresses aligned N-S (and hence, mountain orientations E-W) along the equator ([22]). We therefore consider some simple possibilities of stresses produced by changes in rotation rate.

Stress Equations

We construct models showing fault orientations using the following equations ([*Melosh*(2011)]) which describe the horizontal stress components of the principal stress orientations that develop in a thin, initially unstressed, elastic shell. The horizontal stresses in the north-south (meridional) and east-west (azimuthal) directions are defined as $\sigma_{\theta\theta}$ and $\sigma_{\phi\phi}$, respectively and are given by:

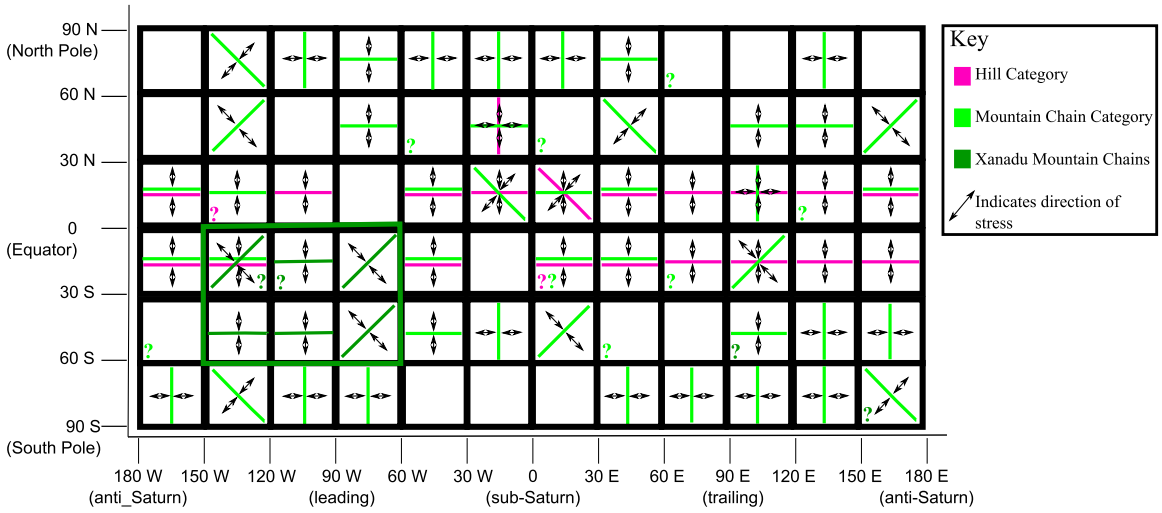

Figure 5.10: A cartoon of the orientations of the mountain chains and hills within a given 30 degree square region and the direction of the stress required to form mountains with the given orientation. The given orientations are based off the rose diagrams shown in Figure 4.8. Like the color scheme of Figure 4.7, bright green lines indicate the orientations for the mountain chain category, pink for the hill category, and dark green for those mountain chains within the Xanadu region. Question marks, which are also color coded as above, indicate that either no orientation can be concluded from the rose diagram for the given region (marked as a question mark in an otherwise blank square) or, an orientation was given however orientation in another direction was also significant. Arrows indicate the direction of stress—can be either compressive or tensile.

$$\sigma_{\theta\theta} = \frac{1}{3}\Delta f \mu (\frac{1+\nu}{5+\nu})(5.0 + 3.0cos[2\theta]), \tag{5.1}$$

$$\sigma_{\phi\phi} = \frac{-1}{3}\Delta f \mu (\frac{1+\nu}{5+\nu})(1.0 - 9.0cos[2\theta]), \tag{5.2}$$

where μ is the rigidity equal to 3.52×10^9 Pa, ν is the Poisson ratio approximated as to 0.314 ([28]), and θ is the angular distance from the axis of symmetry.

f is equal to the flatness (oblateness) of the body and Δf the change in flattening from an initially unstressed state. f is calculated using the Darwin-Radau approximation ([2]),

$$\mathbb{C} = \frac{2}{3}(1 - \frac{2}{5}(\frac{5}{2}\frac{q}{f} - 1)^{\frac{1}{2}}) \tag{5.3}$$

where $\mathbb{C}$, the moment of inertia coefficient, is equal to 0.35 ([7]) and q is the centripetal/gravitational acceleration and equal to

$$q = \frac{\omega^2 R^3}{GM} \tag{5.4}$$

with R, the mean radius, equal to 2576 km, M the mass of the body equaling $1.3452{\times}10^{23}\ kg$, and G the gravitational constant, $6.67284{\times}10^{-11}\ m^3/(kgs^2)$. ω is the rotation rate equal to 2π divided by the period.

All model results shown below used the above equations and a compression-positive sign convention.

Global Expansion/Contraction

Any process that changes the shape or volume of a planet can produce tectonic stress. The largest scale change is an alteration in planetary radius caused by heating or cooling ([*Melosh*(2011)]).

The stresses $\sigma_{\theta\theta}$ and $\sigma_{\phi\phi}$ are equal ([*Melosh*(2011)]) when considering global expansion/contraction, and are therefore equal to

$$\sigma_{\theta\theta} = \sigma_{\phi\phi} = 2\mu\frac{1+\nu}{1-\nu}\frac{\Delta R}{R}, \tag{5.5}$$

where ΔR is the change in radius and is defined as negative for expansion, positive for contraction.

Stresses that result from global expansion or global contraction are isotropic and produce normal faults under the expansion regime and thrust faults under the contraction regime, extending from the equator to the poles. Both stresses are equal

and therefore faulting (and hence, tectonic mountain chains) formed by an expansion/contraction period have no preferred orientations. Therefore, faulting resulting from the change in planetary radius alone, is not a fit for the observed global pattern of mountain chains and hills observed on Titan.

Change in Rotation Rate

Stresses as a result of a change in rotation rate are equal to

$$\Delta\sigma_{\theta\theta} = \sigma_{\theta\theta}(\omega_f) - \sigma_{\theta\theta}(\omega_i), \tag{5.6}$$

$$\Delta\sigma_{\phi\phi} = \sigma_{\phi\phi}(\omega_f) - \sigma_{\phi\phi}(\omega_i), \tag{5.7}$$

where $\sigma_{\theta\theta}(\omega_{f/i})$ and $\sigma_{\phi\phi}(\omega_{f/i})$ are calculated using Equations 5.1 and 5.2 with the initial and final rotation rates, ω_i and ω_f.

We determine fault orientation using Anderson's theory of faulting ([1]). Assigning each of the three principal stresses, σ_1, σ_2, σ_3, to either the north-south stress, the east-west stress, or the vertical stress based on relative magnitudes, we are able to determine whether normal, thrust, or strike-slip faulting occurs at the surface. The vertical stress is related to the weight and density of the overlying ice by ([16]):

$$\sigma_v = \rho g z, \tag{5.8}$$

where z is the distance into the ice shell. For Titan, using the density of ice I (equal to $0.934 g/cm^3$) and a shell thickness of 100 km ([30]), the vertical stress is calculated to be 0.0124 bar/km. Note that the vertical stress is equal to zero at the surface. By definition of the compression-positive convention, σ_1 is vertical in a normal fault regime, σ_2 is vertical in a strike-slip fault regime, and σ_3 is vertical in a

thrust fault regime ([16]). Also, $\sigma_1 > \sigma_2 > \sigma_3$, where σ_1 is most compressive.

Considering initial periods ± half a Titan day, the stress field as a result of a change in rotation rate (spin-up or despinning) is anisotropic within both the equatorial region (extending from $+48^\circ$ to -48°) and the polar regions (extending from $\pm 48^\circ$ to 90°) (Figure 5.11).

As Titan's spin rate changes, strike-slip faults (orientated in a NE-SW and NW-SE conjugate pattern) result in the equatorial region because the principal stress, σ_2, is assigned as the vertical stress. In the polar regions, as the spin rate decreases, normal faulting results from a designation of σ_1 as the vertical stress. The fault orientations (and hence, mountain chain orientations) are in the east-west direction as a result of the more tensile north-south stress, $\sigma_{\theta\theta}$. Similarly, east-west faulting (and hence, mountain chain orientations) result from a increase in Titan's rotation rate. However, the fault type changes from normal to thrust due to the designation of the vertical stress as σ_3. This is the same result reported by [**?**]. The faulting, however, does not match the pattern of mountain chains and hills observed on Titan in either the equatorial nor polar regions.

Expansion/Contraction with Change in Rotation Rate

Next, we model Titan's stress field resulting from global contraction with spin-up and global expansion with despinning, a combination of the two previous models. All changes in planetary radius alter the rate of rotation due to the conservation of angular momentum. In such cases, the resulting horizontal field is everywhere anisotropic (Figure 5.12).

For the expansion with despinning case, the vertical stress is always the principal stress σ_1 and the north-south stress, $\sigma_{\theta\theta}$, the most tensile stress, assigned as σ_3. Therefore, east-west normal faulting (and hence, mountain chain orientation) occur

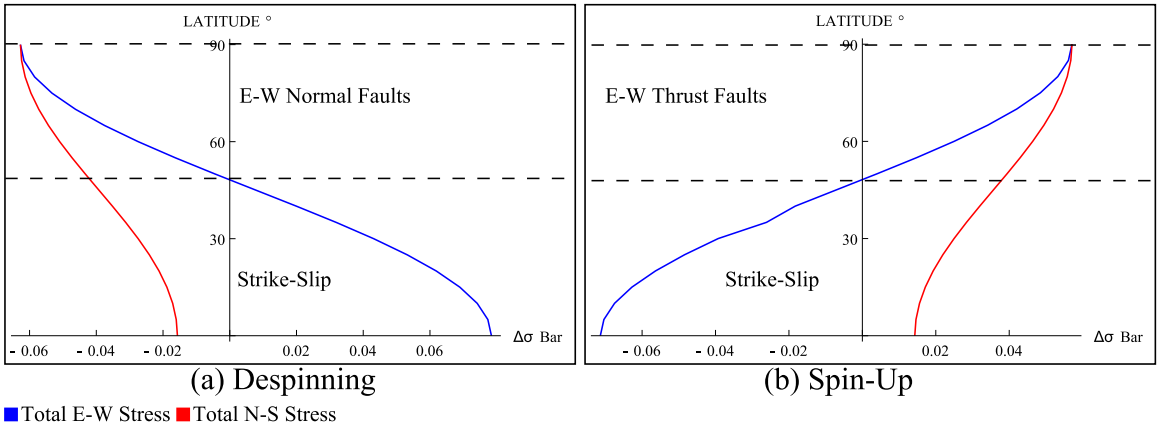

Figure 5.11: The change in spin-rate, $\Delta\sigma$ versus latitude. As Titan's spin rate changes, strike-slip faults (orientated in an NE-SW and NW-SE conjugate pattern) result in the equatorial region as defined by Anderson's theory of faulting when the principal stress, σ_2, is assigned as the vertical stress. As the spin rate decreases, normal faulting results from a designation of σ_1 as the vertical stress in the polar regions (north of 48° latitude). The fault orientations (and hence, mountain orientations) are in the east-west direction as a result of the more tensile north-south stress, $\sigma_{\theta\theta}$. Similarly, east-west faulting (and hence, mountain orientations) result from a increase in Titan's rotation rate. However, the fault type changes from normal to thrust due to the designation of the vertical stress as σ_3.

everywhere except at the poles.

For the contraction with spin-up case, the vertical stress is always the principal stress, σ_3 and the north-south stress, $\sigma_{\theta\theta}$, the most compressive stress, assigned as σ_1. Therefore, east-west thrust faulting (and hence, mountain chain orientation) occur everywhere.

We therefore conclude that these contraction/spin-up and expansion/despinning models do not by themselves explain our observations of Titan's global patterns. It is not apparent that a single model, nor a combination of a change of rotation rate and expansion/contraction, can provide the sources of compression and/or tension needed to form the observed mountain chain orientations; specifically those mountain chains with north-south orientation at the poles.

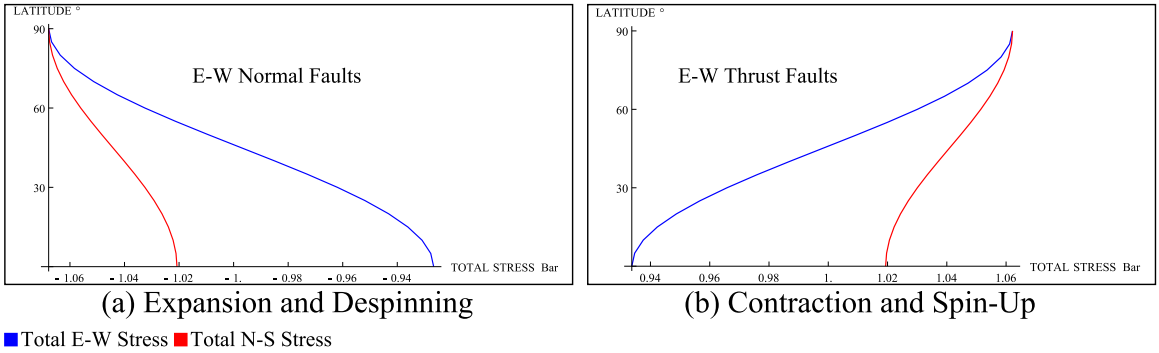

(a) Expansion and Despinning (b) Contraction and Spin-Up

Figure 5.12: Total stress, expansion with despinning and contraction with spin-up versus latitude. In the expansion with despinning case, the vertical stress is always the maximum principal stress σ_1 whereas the north-south stress, $\sigma_{\theta\theta}$, is the minimum stress σ_3. Therefore, east-west normal faulting (and hence, mountain chain orientation) occurs everywhere. In contrast, the contraction with spin-up case, the vertical stress is always the minimum principal stress, σ_3 and the north-south stress, $\sigma_{\theta\theta}$, the most compressive stress, σ_1. Therefore, east-west thrust faulting (and hence, mountain chain orientation) occurs everywhere.

Expansion/Contraction with Change in Rotation Rate with variation of shell thickness

We therefore consider the possibility of nonuniform lithospheric thickness, as explored by [9]. [9] describes the generation of north-south tectonic features in the polar regions of planets through the generation of contraction and spin-up or expansion and despinning with a lithosphere thinner at the poles.

Using the thin shell elastic model and a tension-positive convention, Figure 5.13 is constructed for a generic Titan using a Poisson ratio, ν, of 0.33 and the equator-to-pole thickness ratio of r:

$$r = \frac{h_E}{h_P}, \tag{5.9}$$

with h_E the equatorial thickness and h_P the polar thickness.

The proportion between contraction/expansion and spin rate is parameterized by the contraction/despinning ratio χ:

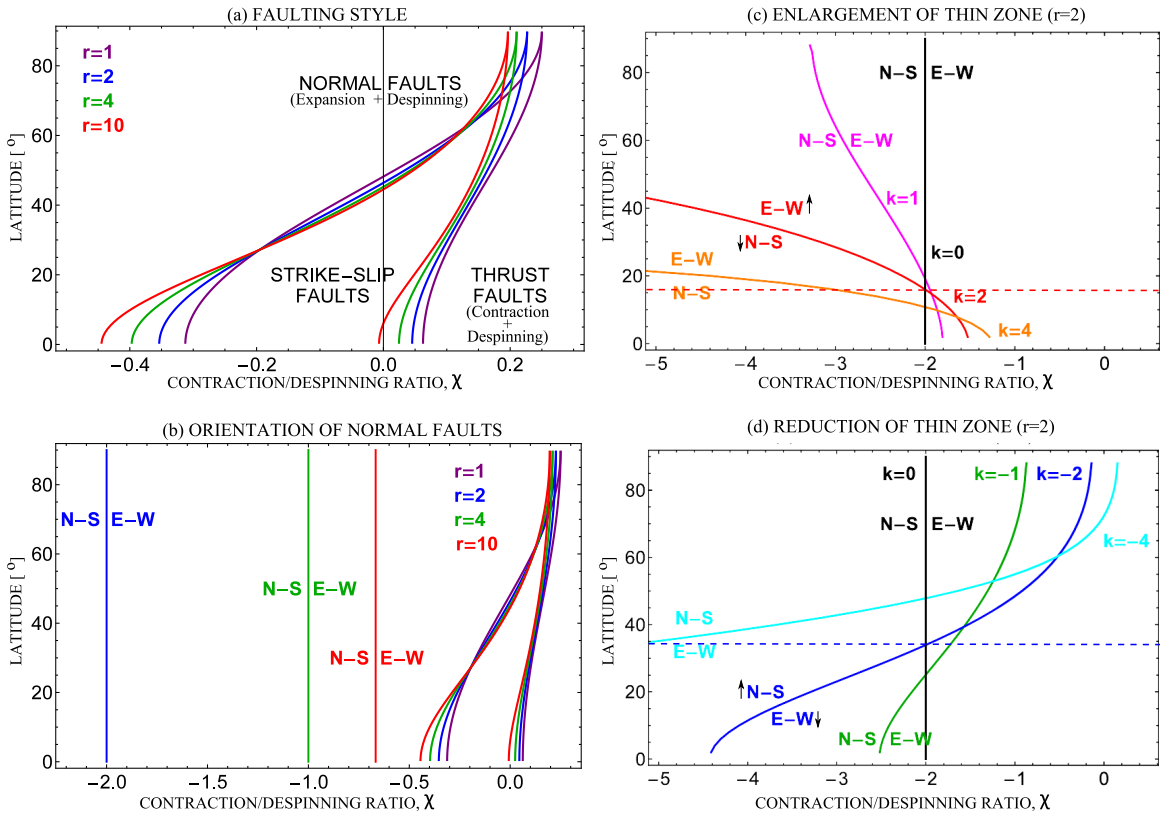

Figure 5.13: Faulting and orientation for simultaneous expansion and despinning for a generic Titan with a Poisson ratio equal to 0.33. a. Boundaries of the areas with a given fault style for a range of ice shell thickness ratios. b. The threshold beyond which the orientation of the normal faults change from north-south to east-west. The threshold for $r = 1$ is at infinity because the thrust faults never switch orientation when the elastic thickness is constant. The boundaries of the areas with a given fault style are shown as in (a). c. Enlargement of the thin zone with $r = 2$. The value k refers to the size of the thin zone. For polar lithospheric thinning, negative values correspond to a reduction and positive values to expansion. A k value equal to zero is the same as the curve mapping $r = 2$ and therefore indicates no expansion or reduction of the thin zone.

$$\chi = -\frac{\bar{w}_0}{\bar{w}_2}, \tag{5.10}$$

which is zero if there is only a change in spin rate and negative when considering either expansion with despinning or contraction with spin-up. $\bar{w}_0$ and $\bar{w}_2$ describe degree-zero and degree-two in the expansion of the nondimensional transverse displacement—the inward and outward motion of the elastic ice shell caused by con-

traction/expansion and spin-up/despinning—with $\bar{w}_0$ describing contraction and $\bar{w}_2$ describing oblateness. Figure 5.13 considers the case of contraction/expansion with despinning when combined with a thin polar lithosphere. Note that when considering contraction/expansion with spin-up, the stress values change sign. Therefore, the resulting model for χ versus latitude is the same curve, but with different faulting styles (i.e. normal faulting in figure 5.13 changes to thrust faulting and thrust faulting on figure 5.13 changes to normal faulting).

Figure 5.13a shows the faulting style of a Titan with simultaneous expansion and despinning. For given χ, the curves indicate the boundaries between the tectonic provinces. Each set of curves is formed by modeling the latitude versus χ using the following equations derived using equations provided in [9]):

$$cos[2\theta] = \frac{\frac{1+4\chi(5+\nu)}{1-\nu}}{9}, \tag{5.11}$$

$$cos[2\theta] = \frac{\frac{-5+4\chi(5+\nu)}{1-\nu}}{3}, \tag{5.12}$$

where θ is the colatitude.

As stated above, a negative χ corresponds to an expansion with despinning event. Using this type of event as an example, as χ decreases due to an increase of $\bar{w}_0$ (i.e., becoming more expansion dominated), the faulting style changes from strike-slip in the equatorial region and normal in the polar region to normal faulting throughout the surface. This is expected and shown in figure 5.12. Note that as r, the equator to pole thickness ratio, increases, the expansion rate must increase in order for fault type to change with latitude.

Titan, however, has a change in fault orientation with respect to latitude. Figure 5.13b shows the threshold beyond which the orientation of the normal faults change from north-south to east-west in the case of expansion with despinning. The thresh-

old for $r = 1$ is at infinity because the normal faults never switch orientation when the elastic thickness is constant. As r increases, however, a latitudinal change in the orientation of faulting does not occur simply by stating the lithospheric thickness is thinner in the polar regions. Any change in normal or thrust fault orientation occurs over all latitudes simultaneously therefore cannot account for the mountain orientations on Titan.

By changing the size of the thin zone, however, such a change in orientation can be achieved (Figure 5.13c and 5.13d). Models c and d of figure 5.13 are shown with an equatorial to polar thickness ratio, $r = 2$ — or in other words, a lithosphere that is two times thicker at the equator than at the poles. The value k refers to the size of the thin zone defined within the interval [0,π/2] that is non-linearly stretched by a function Ψ_k ([9]) equal to:

$$\Psi_k = \frac{\pi}{2}\frac{\sinh(2k\theta)}{\sinh(k)}, if k > 0 or \Psi_k = \frac{\pi}{2}\frac{\sinh(2k\theta)}{\tanh(k)}, if k < 0. \quad (5.13)$$

For polar lithospheric thinning, negative values correspond to a reduction and positive values to expansion. For example, in the case of a reduction of the thin zone, the area defined by the value h_P, the polar lithospheric thickness, decreases in size poleward as the value of k becomes more negative. Note that a k value equal to zero is the same as the curve mapping $r = 2$ and therefore indicates no expansion or reduction of the thin zone ([9]).

Figure 5.13c and 5.13d are interpreted as follows: For $k = 0$ and $\chi = -2$, the resulting fault pattern has no preferred orientation— since both the N-S and E-W stresses are equal. For $k = 2$, corresponding to an enlargement of the thin zone (Figure 5.13c), fault orientation changes latitudinally at the point when the curve intersects a vertical line passing through $\chi = -2$. Therefore, N-S faulting (and hence, mountain chains) occurs equatorward of approximately 15° latitude and E-W

faulting (and hence, mountain chains) occurs poleward of approximately 15° latitude. This pattern is the same for all positive k values, with the exception of the latitudinal position at which they switch orientation. Figure 5.13c, where the thin zone is getting bigger, this "switch position" decreases in latitude as the value of k increases.

For the case of a reduction of the thin zone, N-S faulting (and hence, mountain chains) can form in the polar regions (Figure 5.13d). Consider a k value of -4. The switch to E-W orientated faults (and hence, mountain chains) to N-S orientated faults (and hence, mountain chains) occurs at approximately 35°. As before, this "switch position" increases in latitude as the value of k increases.

It is important to note that if the size of the thin zone varies ($k \neq 0$), a change in fault orientations that is latitude dependent can result, as needed to account for observed mountain chain orientations. Nonetheless, it is also required that the value of $\chi < -0.7$ for the range of $r = 1, 2, 4, 10$. Also, for smaller variability in ice shell thickness from the equator to the poles ($r < 4$), the latitudinal dependent fault change occurs at $\chi < -1$, indicating that the expansion or contraction term dominates over changes in spin rate in controlling latitudinal changes in fault orientation.

Therefore, we have found a theoretical model that matches the observed pattern of mountain chains and hills on Titan — East-west faulting in the equatorial region along with north-south faulting in the polar regions can be explained through the model of global contraction and spin-up or global expansion and despinning combined with a lithosphere in thinner in the polar regions that has a thin zone that is reducing in size (i.e. an area of thinning that is decreasing in size poleward).

Chapter 6 Discussion

While tectonic features can often be formed by local or regional processes, on some icy moons they form a global pattern. The pattern is generally the result of global deformation of the body's ice shell, generating a global stress field that may result in a faulting pattern at the surface ([51]). Mapping of Titan's mountain chains and hills reveals such a global pattern.

We can now place Titan into the small category of solar system bodies with global stress patterns due to the mountain and hill orientations displaying a general pattern of east-west orientation within 30° of the equator, north-south within 30° of the poles, and a mix of both in the 30°-60° latitude range. While we cannot conclude whether Titan's mountains were, or continue to be, formed by contraction or expansion, there is evidence for both throughout the solar system. For instance, the surfaces of Mars, Mercury, and Io show compressional tectonic features whereas many icy satellites, such as Ganymede, Enceladus, and Europa, show evidence of extension and normal faulting.

On Titan, if mountain chain and hill orientations result from thrust faults (resulting from global contraction), then an east-west pattern in the equatorial region is possible if coupled with the spin-up stress field (figure 5.12). However, this pattern is everywhere anisotropic. A change rotation rate can also produce fields of east-west thrust or normal faulting, however, this occurs in the polar regions with strike-slip faulting in the equatorial region. Therefore, neither model can account for the north-south thrust or normal faulting at the poles (Figure 6.14).

It is the unaccounted for north-south orientations in polar regions that lead us to conclude the global stress models in Figures 5.11 and 5.12 do not provide a good fit for explaining the orientations of Titan's mountain chains and hills. This is why we consider a change in the mean planetary radius (contraction or expansion) cou-

pled with planetary flattening due to a change in the rotational period (spin-up or despinning) which can theoretically result in north-south faulting in the polar regions and east-west faulting at the equator, as long as the body's lithosphere has a thin zone that is reducing in the polar regions ([9]) (Figure 6.14). Variation of lithospheric thickness on Titan may have resulted from a tidally-heated, conductive ice shell, as evidenced by topographic mapping ([30]).

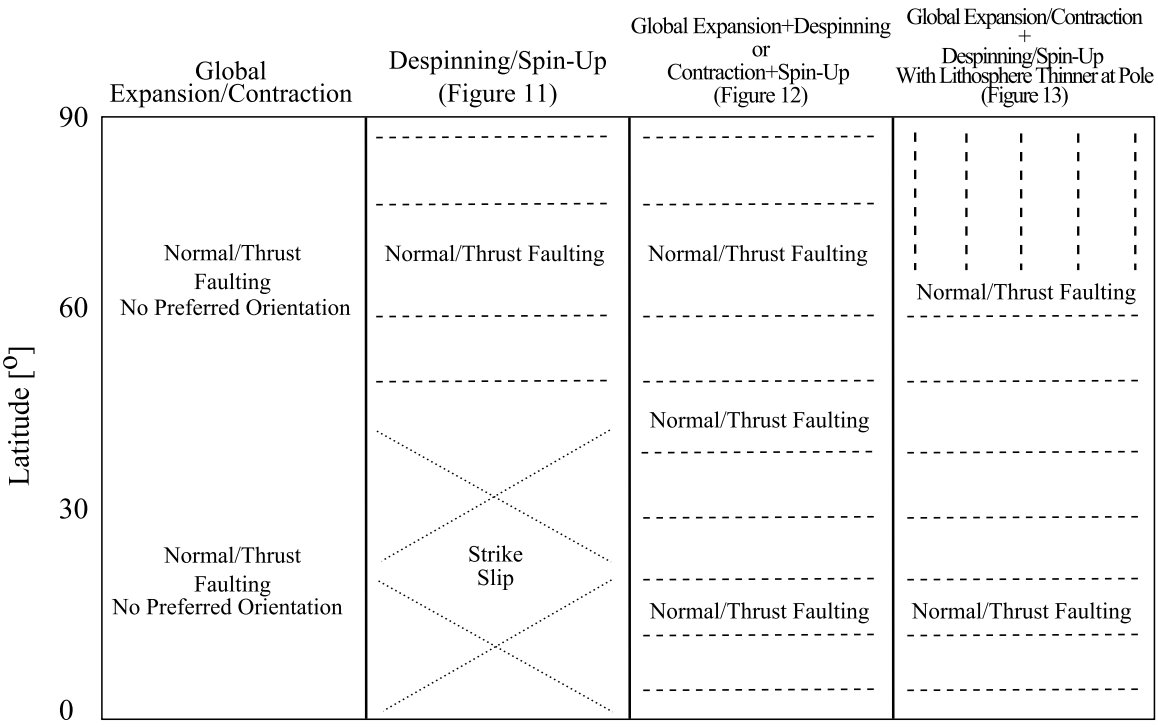

Figure 6.14: Faulting patterns as a result of the various forms of stress illustrated in Figures 5.11, 5.12, and 5.13. We find a match to the observed mountain chain and hill orientations when considering contraction and spin up or expansion and despinning combined with a lithosphere thinner in the polar regions than at the equator. The southern hemisphere reflects that of the northern hemisphere shown in this figure.

Although we suggest that Titan's mountain chains and hills may have been formed through either a combination of global contraction with spin-up or global expansion with despinning and a lithosphere thinner in the polar regions, we recognize that either mechanism may be difficult to achieve.

The spinning-up of Titan can be caused by the body's response to Saturn's grav-

itational pull during its orbital migration at pericenter. However, it is not certain whether the amount of spin-up at pericenter would provide the appropriate amount of stress needed for the thrust faulting to occur. On the other hand, spin-up can be the response to planetary contraction due to the moderate cooling of Titan's low ammonia concentrated ocean— which is what would be expected within the most recent 100 million years (S. Vance, personal communication, 2014).

Similarly, a despinning event on Titan could result from the body's response to Titan's orbital migration outward. As in the case of spin-up, despinning can also be the response to the change of the planetary radius. In this case, however, despinning is the response to the expansion due to the freezing of Titan's ice I shell. On the other hand, global expansion could result from the Titan's despinning early in its history. This is where models for the despinning and expansion of Titan suffer. A high despinning rate, more than what is expected during Titan's outward orbital migration, would be needed for the formation of normal faults ([36]). This rate may have been present early in Titan's history, however, the time it would take for Titan to produce mountain chains and hills is much longer than the relatively short amount of time that it presumably took for Titan to reach its current rotational period.

The above discussion is not to say that global contraction with spin-up nor that global expansion with despinning answers the question in entirety of how Titan's mountain chains and hills were (or are currently) formed. The low stress values used within the models, which are much lower than would be expected for fault formation (but, provide a context for understanding principal stress directions and hence fault orientations), could be swaying the perception of what is occurring within Titan's ice shell. However, liquid hydrocarbons within Titan's ice shell require a much lower stress rate for fault formation and therefore suggest that faults could be more likely in the event that such liquids introduce a fluid pressure that reduces the differential stress needed for frictional failure ([25]).

Also, the models presented in figure 5.13 suggest that the ratio of change in planetary radius to spin-rate, χ, as well as the amount at which the size of the polar thin zone is reducing or expanding, k, influences the orientation of fault (and hence, mountain chain) formation. If either or both parameters have changed within the history of Titan, this may explain the exceptions of mountain chain orientations that occur within both the equatorial and polar regions— as well as the overlap in orientations of mountain chains within the northern and southern mid-latitudes.

Determination of whether Titan is (or has experienced in the past) globally contracting or expanding requires more work. The identification of fault type (thrust faults if contraction, normal faults if expansion) would provide the most useful indication— however, Titan's thick atmosphere and high erosion rate on its surface makes fault identification difficult ([26]).

Chapter 7 Conclusion

Titan's mountain chains and hills form a global pattern: They are preferentially orientated east-west at the equator and north-south at the poles, with overlap in the mid-latitudes. Global stress models that show either tidal response changes or spin rate changes alone cannot account for the faulting pattern (whether thrust or normal) that would be needed to form the observed mountain chains and hills on Titan. We therefore conclude that this pattern may be a result of Titan's ice shell being thinner at the poles while globally contracting and spinning-up or expanding and despinning.

We suggest further observations, such as higher resolution and/or stereo imagery, of the mountain chains and hills in order to conclusively determine Titan's global stress field, during the period of tectonic mountain formation. Better imaging of the mountain chains and hills, perhaps with the use of an airplane mission to Titan ([6]), could help to identify faulting and accurately constrain the stresses responsible for the faulting/tectonics and, hence, provide us with the mechanisms driving mountain formation on Titan.

References

[1] Anderson, E.M., The dynamics of faulting and dyke formation with applications to Britain, Edinburgh: Oliver and Boyd, 1951. Print.

[2] Barnes, J.W. and Fortney, J.J., Measuring the oblateness and rotation of transiting extrasolar giant planets, The Astrophysical Journal **588** (2003) 545–556.

[3] Barnes, J.W., Radebaugh, J., Brown, R.H., Wall, S., Soderblom, L., Lunine, J., Burr, D., Sotin, C., Le Mouelic, S., Rodriguez, S., Buratti, B.J., Clark, R., Baines, K.H., Jaumann, R., Nicholson, P.D., Kirk, R.L., Lopes, R.M.C., Lorenz, R.D., Mitchell, K., and Wood, C.A., Near-infrared spectral mapping of Titan's mountains and channels, Journal of Geophysical Research **112** (2007).

[4] Barnes, J.W., Soderblom, J.M., Brown, R.H.,Buratti, B.J., Sotin, C., Baines, K.H., Clark, R.N., Jaumann, R., McCord, T.B., Nelson, R., Le Moue lic, S., Rodriguez, S., Griffith, C., Penteado, P., Tosi, F., Pitman, K.M.,Soderblom, L., Stephan, K., Hayne, P., Vixie, G., Bibring, J.,Bellucci, G., Capaccionim, F., Cerronim, P., Coradini, A.,Cruikshank, D.P., Drossart, P., Formisano ,V., Langevin, Y., Matson, D.L., Nicholson, P.D., Sicardy, B., VIMS spectral mapping observations of Titan during the *Cassini* prime mission, Planetary and Space Science **57** (2009) 1950–1962.

[5] Barnes, J.W., Bow, J., Schwartz, J., Brown, R.H., Soderblom, J.M., Hayes, A.G., Vixie, G., Le Mouelic, S., Rodriguez, S., Sotin, C., Jaumann, R., Stephan, K., Soderblom, L.A., Clark, R.N., Buratti, B.J., Baines, K.H., Nicholson, P.D., Organic sedimentary deposits in Titan's dry lakebeds: Probable evaporite, Icarus **216** (2011) 136–140.

[6] Barnes, J.W., Lemke, L. Foch, R., McKay, C.P., Beyer, R.A., Radebaugh, J. Atkinson, D.H., Lorenz, R.D., Le Mouelic, S., Rodriguez, S., Gundlach, J., Gi-

annini, F., Bain, S., Flasar, F.M., Hurford, T., Anderson, C.M., Merrison, J., Adamkovics, M., Kattenhorn, S.A., Mitchell, J., Burr, D.M., Colaprete, A., Schaller, E., Friedson, A.J., Edgett, K.S., Coradini, A., Adriani, A., Sayanagi, K.M., Malaska, M.J., Morabito, D., Reh, K., AVIATR—Aerial Vehicle for In-situ and Airborne Titan Reconnaissance, Experimental Astonomy **33** (2012) 55–127.

[7] Barr, A.C., Citron, R.I., and Canup, R.M., Origin of a partially differentiated Titan, Icarus **209** (2010) 858–862.

[8] Bart, G.D., Turtle, E.P., Jaeger, W.L., Keszthelyi, L.P., Greenberg, R., Ridges and tidal stress on Io, Icarus **169** (2004) 111–126.

[9] Beuthe, M., East-West faults due to planetary contraction, Icarus **209** (2010) 795–817.

[10] Bland, M.T. and Showman, A.P., The formation of Ganymede's grooved terrain: Numerical modeling extensional necking instabilities, Icarus **189** (2007) 439–456.

[11] Brown, R.H., Barnes, J.W., Melosh, H.J., On Titan's Xanadu region, Icarus **214** (2011) 556–560.

[12] Buratti, B.J., Sotin, C., Lawrence, K., Brown, R.H., Le Mouelic, S., Soderblom, J.M., Barnes, J., Clark, R.N., Baines, K.H., and Nicholson, P.D., A newly discovered impact crater in Titan's Senkyo: Cassini VIMS observations and comparison with other impact features, Planetary and Space Science **60** (2012) 18–25.

[13] Burr, D.M., Drummond, S.A., Cartwright, R., Black, B.A., and Perron, J.T., Morphology of Fluvial Networks in Titan: Evidence for Structural Control, Icarus **226** (2013) 742–759.

[14] Collins, G.C., McKinnon, W.B., Moore, J.M., Nimmo, F., Pappalardo, R.T., Prockter, L.M., Schenk, P.M., Tectonics of the outer planet satellites, Planetary Tectonics (2009) 264–350.

[15] Elachi, C., Wall, S., Allison, M., Anderson, Y., Boehmer, R., Callahan, P., Encrenaz, P., Flameni, E., Francescetti, G., Gim, Y., Hamilton, G., Hensley, S., Janssen, M., Johnson, W., Kelleher, K., Kirk, R., Lopes, R., Lorenz, R., Lunine, J., Muhleman, D., Ostro, S., Paganelli, F., Picardi, G., Posa, F., Roth, L., Seu, R., Shaffer, S., Soderblom, L., Stiles, B., Stofan, E., Vetrella, S., West, R., Wood, C., Wye, L., Zebker, H., Cassini RADAR views the surface of Titan, Science **308** (2005) 970–974.

[16] Fossen, H. *Structural Geology.* New York: Cambridge University Press. 2010. Print.

[17] Garcia, A., Rodriguez, S., Le Gall, A., Courrech du Pont, S., Narteau, C., Le Mouelic, S., Lucas, A., Radebaugh, J., Arnold, K., Barnes, J.W., Sotin, C., Brown, R.H., Lorenz, R.D., Turtle, E.P., Global mapping and characterization of Titans dune fields with Cassini: correlation between RADAR and VIMS observations, Lunar Planet. Sci. Conf. 44th. Lunar and Planetary Institute **Houston. Abstract 1719** (2013) 1978.

[18] Geissler, P.E., Greenberg, R., Hoppa, G., McEwen, A., Tufts, R., Phillips, C., Clark, B., Ockert-Bell, M., Helfenstein, P., Burns, J., Veverka, J., Sullivan, R., Greeley, R., Pappalardo, R.T., Head, J.W., Belton, M.J.S., Denk, T., Evolution of lineaments on Europa: clues from Galileo multispectral imaging observations, Icarus **135** (1998) 107-126.

[19] Greenberg, R., Geissler, P., Hoppa, G., Tufts, B.R., Durda, D.D., Pappalardo, R., Head, J.W., Greeley, R., Sullivan, R., Carr, M.H., Tectonic processes on

Europa: tidal stresses, mechanical response, and visible features, Icarus **135** (1998) 64-78.

[20] Golombek, M.P., Constraints on the expansion of Ganymede and the thickness of the lithosphere, J. Geophys. Res. **87A** (1982) 77-83.

[21] Kattenhorn, S.A., Nonsynchronous rotation evidence and fracture history in the Bright Plains region, Europa, Icarus **157** (2002) 582–602.

[22] Kattenhorn, S.A. and Hurford, T., Tectonics of Europa, In: Europa, Pappalardo, R.T., McKinnon, W.B., Khurana, K., eds **University of Arizona Press** (2009) 199-236.

[23] Langhans, M., Lunine, J.I., Mitri, G., Titan's Xanadu region: Geomorphology and formation scenario, Icarus **223** (2013) 796–803.

[24] Le Mouelic, S., Paillou, P., Janssen, M.A., Barnes, J.W., Rodriguez, S., Sotin, M., Brown, R.H., Baines, K.H., Buratti, B.J., Clark, R.N., Crapeau, M., Encrenaz, P.J., Jaumann, R., Geudtner, D., Paganelli, F., Soderblom, L.A., Tobie, G., and Wall, S., Mapping and interpretation of Sinlap crater on Titan using Cassini VIMS and RADAR data, Journal of Geophysical Research **113** (2006).

[25] Liu, Z., Radebaugh, J., Harris, R.A., and Christiansen, E.H., Role of Fluids in Mechanics of Overthrust Faulting on Titan, Paper presented at AGU, San Francisco, Ca, USA (2013).

[26] Lopes, R.M.C., Stofan, E.R., Peckyno, R., Radebaugh, J., Mitchell, K.L., Mitri, G., Wood, C.A., Kirk, R.L., Wall, S.D., Lunine, J.L., Hayes, A., Lorenz, R., Farr, T., Wye, L., Craig, J., Ollerenshaw, R.J., Janssen, M., LeGall, A., Paganelli, F., West, R., Stiles, B., Callahan, P., Anderson, Y., Valora, P., Soderbloom, L., and the Cassini RADAR Team, Distribution and interplay of geologic processes on Titan from Cassini RADAR data, Icarus **205** (2010) 540–558.

[27] Lorenz, R.D., Stiles, B.W., Aharonson, O., Lucas, A., Hayes, A.G., Kirk, R.L., Zebker, H.A., Turtle, E.P., Neish, C.D., Stofan, E.R., Barnes, J.W., and the Cassini RADAR Team, A global topographic map of Titan, Icarus **225** (2013) 367–377.

[*Melosh*(2011)] Melosh, H.J. *Planetary Surface Processess.* New York: Cambridge Planetary Science, 2011. Print.

[28] Mitri, G., Bland, M.T., Showman, A.P., Radebaugh, J., Stiles, B., Lopes, R.M.C., Lunine, J.I., and Pappalardo, R.T., Moutains on Titan: Modeling and observations, Journal of Geophysical Research **115** (2010).

[29] Neish, C.D. and Lorenz, R.D, Titan's global crater population: A new assessment, Planetary and Space Science **60** (2012) 26–33.

[30] Nimmo, F. and Bills, B.G., Shell thickness variations and the long-wavelength topography of Titan, Icarus **208** (2010) 896–904.

[31] Paganelli, F., Janssen, M.A., Stiles, B., West, R., Lorenz, R.D., Lunine, J.I., Wall, S.D., Callahan, P., Lopes, R.D., Stofan, E., Kirk, R.L., Johnson, W.T.K., Roth, L., Elachi, C., the Radar Team, Titan's surface from Cassini RADAR SAR and high resolution radiometry data of the first five flybys, Icarus **191** (2007) 211–222.

[32] Pappalardo, R.T., Head, J.W., Collins, G.C., Kirk, R.L., Neukum, G., Oberst, J., Giese, B., Greeley, R., Chapman, C.R., Helfenstein, P., Moore, J.M., McEwen, A., Tufts, B.R., Senske, D.A., Breneman, H.H., Klaasen, K., Grooved terrain on Ganymede: First results from Galileo high resolution imaging, Icarus **135** (1998) 276-302.

[33] Pappalardo, R.T., Head, J.W., Sherman, N.D., Greeley, R., Sullivan, R.J., the Galileo Imaging Team, Classification of Europan ridges and troughs and a pos-

sible genetic sequence, In: Proc. Lunar Planet. Sci. Conf. 29th. Lunar and Planetary Institute **Houston. Abstract 1859 [CD-ROM]** (1998).

[34] Patthoff, D.A. and Kattenhorn, S.A., A fracture history on Enceladus provides evidence for a global ocean, Geophysical Research Letters **38** (2011).

[35] Peale, S.J., Rotation histories of the natural satellites, Planetary Satellites **ed.J.A. Burns (Tucson: Univ. Arizona Press)** (1977) 87–112.

[36] Pechmann, J.B. and Melosh, H.J., Global fracture patterns of a despun planet: Application to Mercury, Icarus **38** (1979) 243–250.

[37] Porco, C.C., Helfenstein, P., Thomas, P.C., Ingersoll, A.P., Wisdom, J., West, R., Neukum, G., Denk, T., Wagner, R., Roatsch, T., Kieffer, S., Turtle, E., McEwen, A., Johnson, T.V., Rathbun, J., Veverka, J., Wilson, D., Perry, J., Spitale, J., Brahic, A., Burns, J.A., DelGenio, A.D., Dones, L., Murray, C.D., Squyres, S., Cassini observes the active south pole of Enceladus, Science **311** (2006) 43-64.

[38] Prockter, L.M., Lopes, R.M.C., Giese, B., Jaumann, R., Lorenz, R.D., Pappalardo, R.T., Patternson, G.W., Thomas, P.C., Turtle, E.P., Wagner, R.J., Characteristics of Icy Surfaces, Space Science Review **153** (2010) 63–111.

[39] Radebaugh, J., Lorenz, R.D., Kirk, R., Lunine, J., Stofan, E.R., Lopes, R.M.C., Wall, S.D., and the Cassini Radar Team, Mountains on Titan observed by Cassini Radar, Icarus **192** (2007) 77–91.

[40] Radebaugh, J., Lorenz, R.D., Wall, S.D., Kirk, R.L., Wood, C.A., Lunine, J.I., Stofan, E.R., Lopes, R.M.C., Valora, P., Farr, T.G., Hayes, A., Stiles, B., Mitri, G., Zebker, H., Janssen, M., Wye, L., LeGall, A., Mitchell, K.L., Paganelli, F., West, R.D., Schaller, E.L., The Cassini Radar Team, Regional geomorphology and history of Titan's Xanadu province, Icarus **211** (2011) 672–685.

[41] Smith-Konter, B. and Pappalardo, R.T., Tidally driven stress accumulation and shear failure of Enceladus's tiger stripes, Icarus **198** (2008) 435–451.

[42] Schubert, G., Hussmann, H., Lainey, V., Mutson, D.I., McKinnon, W.B., Sohl, F., Sotin, C., Tobie, G., Turrini, D., Van Hoolst, T., Evolution of Icy Satellites, Space Science Review **153** (2010) 447–484.

[43] Schulson, E.M., The Fracture of Ice Ih, J. Phys. (Paris) **48** (1987) 207–218.

[44] Soderblom, J.M., Brown, R.H., Soderblom, L.A., Barnes, J.W., Jaumann, R., Le Mouelic, S., Sotin ,C., Stephan, K., Baines, K.H., Buratti, B.J., Clark, R.N., and Nicholson, P.D., Geology of the Selk crater region on Titan from Cassini VIMS observations, Icarus **208** (2010) 905–912.

[45] Sohl, F.,Hussman, H., Schwentker, B., Spohn, T., and Lorenz, R.D., Interior structure models and tidal Love numbers of Titan, Journal of Geophysical Research **108** (2003).

[46] Solomonidou, A., Bampasidis, G., Hirtzig, M., Coustenis, A., Kyriakopoulos, K., St. Seymour, K., Bratsolis, E., and Moussas, X., Morphotectonic features on Titan and their possible origin, Planetary and Space Science **77** (2013) 104–117.

[47] Spencer, J.R., Pearl, J.C., Segura, M., Flasar, F.M., Mamoutkine, A., Romani, P., Buratti, B.J., Hendrix, A.R., Spilker, L.J., Lopes, R.M.C., Cassini encounters Enceladus: Background and the discovery of a south polar hot spot, Science **311** (2006) 1401-1405.

[48] Spitale, J., Porco, C., Association of the jets of Enceladus with the warmest regions on its south-polar fractures, Science **449** (2007) 695-697.

[49] Squyres, S.W., The evolution of tectonic features on Ganymede, Icarus **52** (1982) 545-559.

[50] Stiles, B.W., Hensley, S., Gim, Y., Bates, D.M., Kirk, R.L., Hayes, A., Radebaugh, J., Lorenz, R.D., Mitchell, K.L., Callahan, P.S., Zeblcer, H., Johnson, W.T.K., Veeramacheneni, C., and the Cassini RADAR Team, Determining Titan surface topography from Cassini SAR data, Icarus **202** (2009) 584–598.

[51] Vening-Meinesz, F.A., Shear patterns of the Earth's crust, Trans. Am. Geophysics Union **28** (1947) 1–61.